### **PAPER**

## High-efficiency ultra-broadband orbital angular momentum beam generators enabled by arrowbased fractal metasurface

To cite this article: Yiting Liu et al 2021 J. Phys. D: Appl. Phys. 54 475105

View the article online for updates and enhancements.

### You may also like

- Ultrathin broadband acoustic reflection metasurface based on meta-molecule <u>clusters</u> Y B Wang, C R Luo, Y B Dong et al.

- Metasurface design by a Hopfield network: finding a customized phase response in a

Ruichao Zhu, Tianshuo Qiu, Jiafu Wang et

- Coupling-inspired metasurfaces for polarization-correlation customizable

Yongfeng Li, Yongqiang Pang, Lin Zheng



# IOP ebooks™

Bringing together innovative digital publishing with leading authors from the global scientific community.

Start exploring the collection-download the first chapter of every title for free.

J. Phys. D: Appl. Phys. 54 (2021) 475105 (7pp)

https://doi.org/10.1088/1361-6463/ac2201

# High-efficiency ultra-broadband orbital angular momentum beam generators enabled by arrow-based fractal metasurface

Yiting Liu<sup>1</sup>, Rensheng Xie<sup>1</sup>, Xu Chen<sup>2</sup>, Hualiang Zhang<sup>3</sup> and Jun Ding<sup>1,\*</sup>

E-mail: jding@ee.ecnu.edu.cn

Received 8 May 2021, revised 24 August 2021 Accepted for publication 27 August 2021 Published 10 September 2021



### **Abstract**

Vortex beams carrying orbital angular momentum (OAM) are of great importance owing to the capacity to expand channel capacity of communication systems from microwave to optical regimes. In this work, a single-layer ultra-broadband meta-atom is designed by using the method of fractal. The reflected co-polarization amplitude of the arrow-based fractal meta-atom can exceed 0.9 in a frequency range from 6 to 19.7 GHz and the complete  $2\pi$  phase control can be achieved by rotating the structure. Based on the proposed meta-atom, metasurface-based vortex beam generators are designed. As an illustrative example, a metasurface-based OAM beam generator with a mode of +1 is designed, fabricated, and measured. Both the experimental and simulated results match well with each other, proving the practicability of the proposed high-efficiency ultra-broadband metasurface.

Keywords: fractal, metasurface, ultra-broadband, high-efficiency, OAM beam generator

(Some figures may appear in colour only in the online journal)

### 1. Introduction

Vortex beams carrying orbital angular momentum (OAM) have attracted considerable attentions for their promising applications in modern wireless communication systems [1–5]. A vortex beam with the phase factor of  $e^{il\theta}$  carries the OAM of  $l\hbar$  per photon, where  $\theta$  is the azimuthal angle and l represents the OAM mode number. The orthogonality of different OAM modes could provide an additional degree of freedom for the signal modulation [1, 6], enhancing data capacity in different frequency regimes [7–11]. Therefore, a number of traditional methods to generate OAM beams have

been proposed in the past decades [12], such as spiral phase plates [13–17], spatial light modulators [18–21], vortex lasers [22, 23] and uniform circular antenna arrays [24, 25], which typically suffer from the issues such as bulky configurations, low efficiencies as well as narrow bandwidths.

Metasurfaces, the two-dimensional counterparts of the metamaterials, have sparked enormous interest in recent years [26–35] due to their superior capabilities for wavefront modulations. Metasurfaces are composed of low-profile artificially periodic subwavelength structures, demonstrating strong capabilities to manipulate electromagnetic (EM) wavefront [36–39]. Very recently, several metasurfaces have been reported to realize broadband OAM beams, showing broader bandwidth and higher efficiency than the traditional methods [40–45]. An effective approach is based on transmission-type

<sup>&</sup>lt;sup>1</sup> Key Laboratory of Polar Materials and Devices, Department of Electronic Sciences, School of Physics and Electronic Sciences, East China Normal University, Shanghai 200241, People's Republic of China

<sup>&</sup>lt;sup>2</sup> Shanghai Radio Equipment Research Institute, Shanghai 200090, People's Republic of China

<sup>&</sup>lt;sup>3</sup> Department of Electrical and Computer Engineering, The University of Massachusetts Lowell, Lowell, MA 01854, United States of America

<sup>\*</sup> Author to whom any correspondence should be addressed.

metasurface with metallic grating layers [40], which could realize high transmission efficiency in the entire operation band. Moreover, a bilayer reflection-type OAM metasurface is proposed to function in a broad bandwidth from 6.95 to 18 GHz (a fractional bandwidth of 82%,  $r_{co} > 0.89$ ) [41]. Nevertheless, the multilayer structures of the metasurface increase the profile thickness and fabrication complexity. Therefore, single-layer broadband OAM metasurfaces have been reported to tackle these issues, such as the rectangular-hole metasurface [42], the reflection-type brick-shpaed metasurface [43], the ultra-thin z-shaped metasurface [44], and the H-shaped metasurface [45]. Moreover, a novel square-loop-shaped metasurface has achieved the balance between high efficiency and broad bandwidth, with the fractional bandwidth of 105.6%  $(r_{co} > 0.9)$  [46–48]. Furthermore, the fractal topology provides a novel and efficient method to meet the growing requirement of high-efficiency broadband OAM generation [49], which deserves further research.

In this work, a novel ultra-broadband high-efficiency OAM generator based on a fractal metasurface is proposed. Numerical analysis of the proposed arrow-based fractal meta-atom is carried out, and the co-polarization reflection coefficients under the circularly polarized incidence can exceed 0.9 in an ultra-broad working range from 6 to 19.7 GHz with a fractional bandwidth of 107%. The meta-atom is then utilized to design metasurface-based OAM generators based on the Pancharatnam-Berry principle [50, 51]. High-efficiency ultra-broadband OAM beam generators with different topological charges are designed and numerically studied, validating the performance of the designed meta-atom. In addition, an OAM beam generator with a topological charge of +1 is fabricated and characterized, featuring high efficiency and ultra-broad bandwidth. The proposed OAM metasurfaces with high efficiency and broad frequency band could pave the way to enhance the data capacity for wireless communication systems.

### 2. Design of the ultrabroadband meta-atom

Figures 1(a) and (b) plot the top and side views of the proposed reflective meta-atom, which is composed of single-layer metallic structures and a dielectric spacer backed by a ground plane. The top metallic layer of the meta-atom is an arrowbased fractal structure, which is generated from a rectangle bar in the design process of the fractal design. With the rotation angle of the metallic fractal structure  $\theta_r$  modified, the full  $2\pi$  geometric phase control can be achieved with high efficiency under the circular polarization (CP) incidence. The dielectric spacer is made of F4B, with a relative dielectric constant of 2.2 and a loss tangent of 0.002. In the simulations, the thickness of metallic layer is 0.035 mm, the thickness of F4B substrate is  $h_{\text{sub}} = 4$  mm, and the period of the meta-atom is p = 8 mm. The arrow-based fractal consists of rectangle bars with different geometric parameters. The shaft length of the arrow-based fractal is  $l_1 = 7$  mm and the arm lengths are  $l_2 = 3.5$  mm and  $l_3 = 0.85$  mm. The widths of the rectangle bars are  $w_1 = 0.5$  mm,  $w_2 = 0.2$  mm, and  $w_3 = 0.3$  mm.

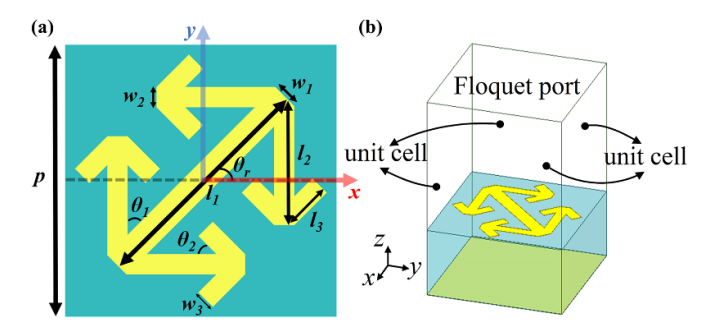


**Figure 1.** The layouts of the proposed meta-atom. (a) Top view. (b) Perspective view.

These rectangle bars are connected at angles  $\theta_1 = 60^{\circ}$  and  $\theta_2 = 30^{\circ}$ .

To analyse the reflected fields for the proposed meta-atom, the reflected Jones matrix can be employed. Reflection coefficients in the Jones matrix under CP incidences are defined as follows [41]:

$$r_{--} = \frac{1}{2} [(r_{xx} - r_{yy}) + j(r_{xy} + r_{yx})] e^{-j2\theta}$$
 (1)

$$r_{++} = \frac{1}{2}[(r_{xx} + r_{yy}) + j(r_{yx} - r_{xy})]e^{j2\theta}$$
 (2)

$$r_{-+} = \frac{1}{2}[(r_{xx} + r_{yy}) + j(r_{yx} - r_{xy})]$$
 (3)

$$r_{+-} = \frac{1}{2} [(r_{xx} + r_{yy}) - j(r_{yx} - r_{xy})]$$
 (4)

where  $r_-$  and  $r_+$  denote the amplitudes of the co-polarized and cross-polarized reflection coefficients of the EM propagation under the left-handed CP (LHCP,—) incidence, respectively, while  $r_{++}$  and  $r_{-+}$  represent the amplitudes of the co-polarized and cross-polarized reflection coefficients under the right-handed CP (RHCP, +) incidence, respectively. Besides,  $r_{xx}$  and  $r_{yy}$  are the amplitudes of the co-polarized reflection coefficients under the x- and y-polarization incidences, respectively. It can be seen from equations (1) and (2) that an abrupt phase change  $e^{-j2\theta}$  ( $e^{j2\theta}$ ) could be introduced in by rotating the meta-atom with an angle of  $\theta$ . Meanwhile, the polarization conversion rate (PCR) of the co-polarization reflection for the LHCP incidence could be used to show the polarization conversion efficiency of the proposed meta-atom. The PCR is defined as

$$PCR = \frac{r_{--}^2}{r_{--}^2 + r_{+-}^2}.$$
 (5)

The proposed meta-atom is numerically studied and analysed by using the commercial software CST Microwave Studio. The boundary conditions in both x- and y-directions are 'unit cell', and a Floquet port is adopted in the z-axis direction. The frequency domain solver is used in the simulation. Figures 2(a) and (b) plot the amplitudes of the reflection coefficients and co-polarized reflection phases with varied rotation angle  $\theta_r$ . As

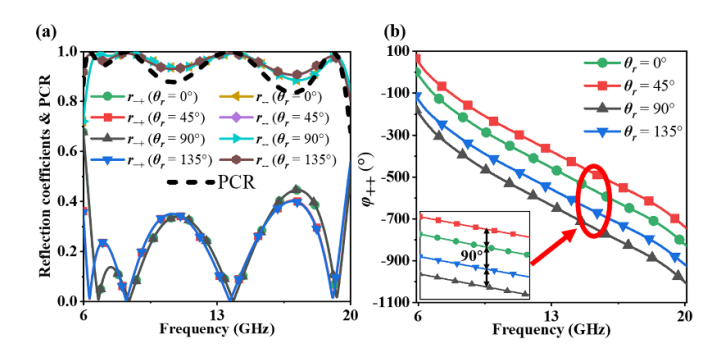


**Figure 2.** The amplitude and phase responses of the reflection coefficients of the proposed meta-atom with varied rotation angle  $\theta_r$  under the RHCP incidence. (a) The amplitudes of the reflection coefficients. (b) The phases of the co-polarized reflection coefficients.

can be seen in figure 2(a), the amplitudes reveal polarization conversion for right-hand circularly polarized incidence in the frequency band ranging from 6 to 20 GHz. The amplitudes of co-polarized reflection coefficients keep higher than 0.9 within the ultrawide frequency range with a fractional bandwidth of 107.2%, and the cross-polarized ones are suppressed. The PCR value of the co-polarization reflection for the LHCP incidence is also shown in figure 2(a), which is higher than 0.8 in the working frequency band. Figure 2(b) exhibits the gradient phase variation by rotating the top metallic structure  $\theta_r$  with an interval of 45°. It can be seen from figure 2(b) that the phase variation is almost twice the rotation angle  $\theta_r$  in an ultrawide bandwidth from 6 to 20 GHz. Figure 2 indicates that the ultra-broadband phase manipulation with high efficiency can be achieved by simply rotating the proposed metaatom under the CP incidences. In order to study the method of the fractal structure, figures 3(a)-(c) demonstrate the evolution progress of the original bar structure (stage 1) shown in figure 3(a). The arrow structure shown in figure 3(b) can be obtained by adding two parasitic bars at each end of the bar structure, and the adding operation can be repeated to spawn higher order iterations. Consequently, the reflection performances of the optimized three fractal stages are presented in figure 3(d). For the original structure (stage 1), the amplitude of the co-polarized reflection coefficient keeps higher than 0.9 in a relatively narrow range of 18.3-19.7 GHz with a fractional bandwidth of only 7.4%. The first-level arrow-based fractal structure (stage 2) could achieve an enlarged bandwidth, from 8.4 to 19 GHz with a fractional bandwidth of 77.4%. Finally, the ultra-wide bandwidth from 6 to 19.7 GHz with a fractional bandwidth of 107.2% can be obtained by the proposed metaatom (stage 3). Compared with other stages, the fractal design of the stage 3 achieves a good balance between high amplitude and wide operating bandwidth.

### 3. Designs of metasurface-based OAM generators

OAM beam generators based on the arrow-based fractal metasurface are studied in this part. The phase distribution of the OAM metasurface can be expressed as [52]

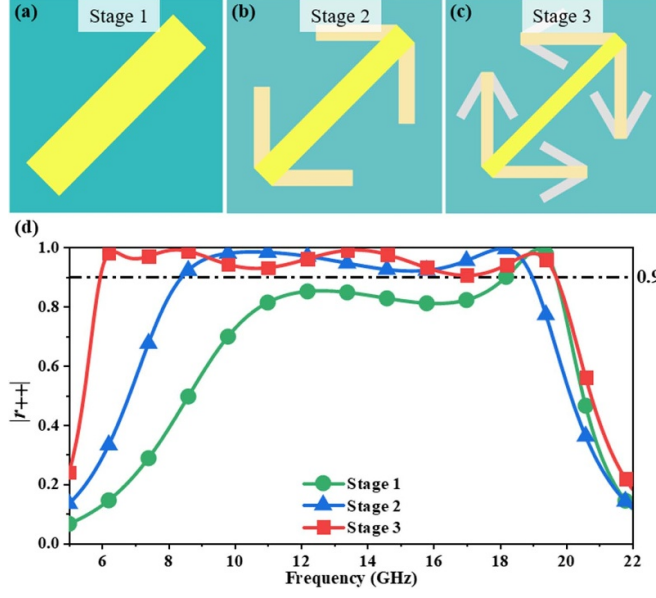


**Figure 3.** The design process of the fractal structure. (a)–(c) The schematic views of stage 1–3. The added rectangles in every stage are painted in different colors. (d) The simulated amplitude of co-polarized reflection coefficients in stage 1–3.

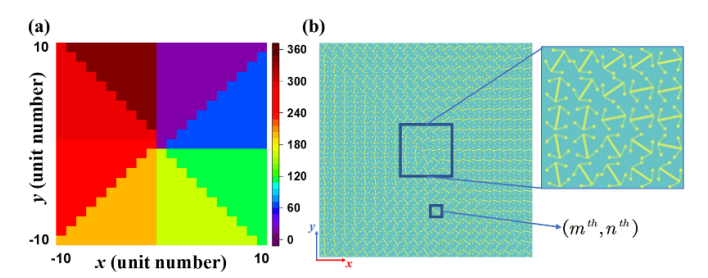


**Figure 4.** (a) The calculated phase distribution and (b) the layouts of the OAM metasurface  $(21 \times 21)$  with l = +1.

$$\varphi(m,n) = l \tan^{-1} \left(\frac{n}{m}\right) \tag{6}$$

where l denotes the topological charge of the vortex beam, m and n represent the position coordinates of the (mth, nth) meta-atom in the x- and y-directions, respectively. Figure 4(a) demonstrates the phase distribution of the proposed OAM metasurface with a topological charge of +1 and an array of  $21 \times 21$  meta-atoms. As can be seen from figure 4(a) that the phase distribution changes by  $360^{\circ}$  for a full turn circling the propagation axis. The metasurface is composed of  $21 \times 21$  meta-atoms covering a total area of  $168 \times 168$  mm<sup>2</sup>, which is shown in figure 4(b). Figure 4(b) also shows an enlarged part of the centre  $5 \times 5$  meta-atoms.

Then, the full-wave simulations by CST Studio Suite are conducted to investigate the proposed OAM metasurface in the frequency range from 6 to 20 GHz. Figure 5 plots the simulated intensity and the phase distributions of the RHCP field ( $E_{\rm R}$ ) at 6, 10, 12, 14, 16, 18, and 20 GHz under RHCP plane wave excitation. The incident plane waves are sampled at a distance z=300 mm from the vortex beam generator.

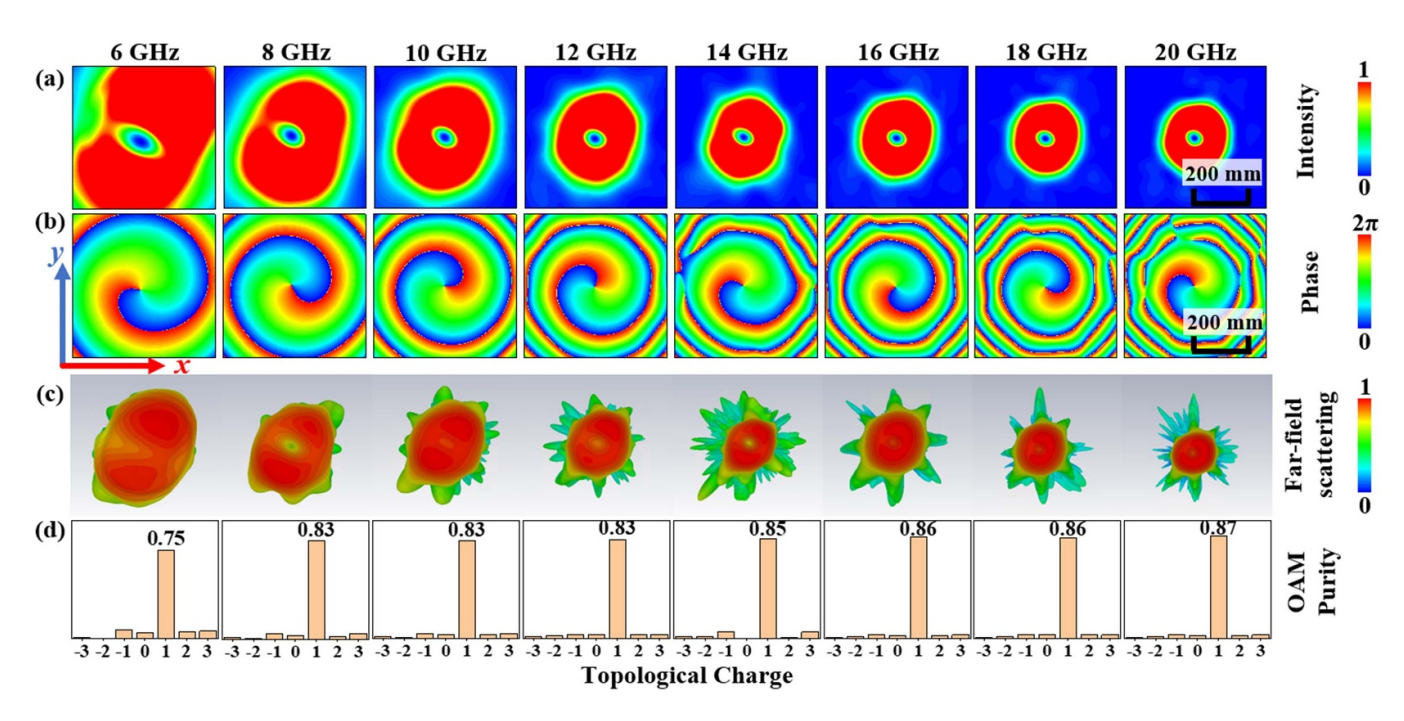


Figure 5. The simulated results of the OAM metasurface with l = +1 from 6 to 20 GHz with a step of 2 GHz. (a) Intensity, (b) phase distributions, (c) far-field scattering patterns, and (d) the calculated OAM purities.

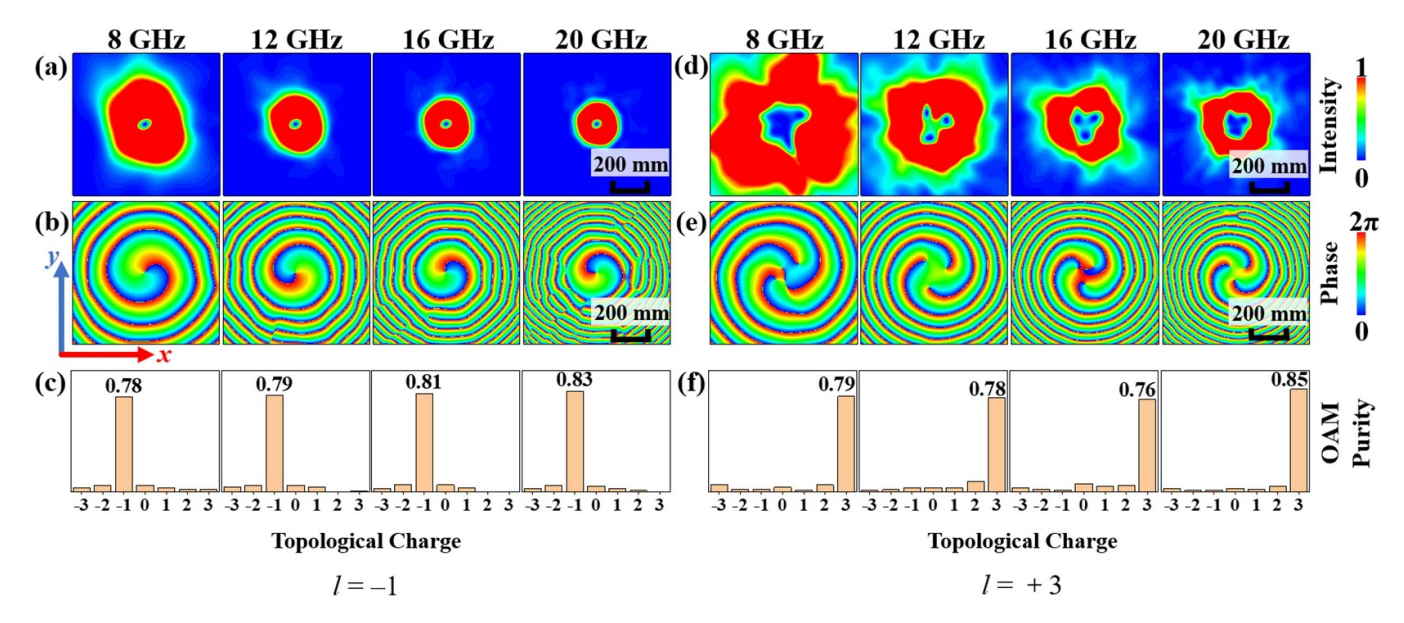
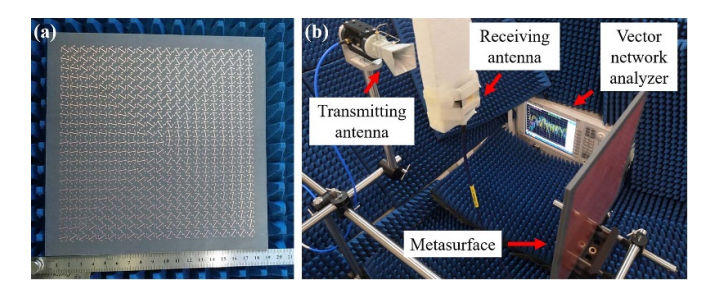


Figure 6. The simulated results of the OAM metasurfaces with l = -1 from 8 to 20 GHz with a step of 4 GHz. (a) Intensity, (b) phase distributions, and (c) OAM purities in the *xoy* plane. The simulated results of the OAM metasurfaces with l = +3 from 8 to 20 GHz with a step of 4 GHz: (d) intensity, (e) phase distributions, and (f) OAM purities in the *xoy* plane.

All the patterns in figures 5(a) and (c) are normalized values. Figure 5(a) shows the intensity distributions of the  $E_R$  and the characteristic amplitude nulls resulted from the phase singularity exist at the central regions, which can be also observed in the far-field patterns shown in figure 5(c). In figure 5(b), it is found that the major feature of the spiral phase distributions is obtained, and its phase characteristics of topological charge l = +1 can be well recognized. Furthermore, the concept of OAM spectrum could be introduced

for numerically quantitative exploration of the OAM mode purity. The fast Fourier transform algorithm is adopted in the calculation of OAM spectrum and the Fourier transform analysis of OAM mode purity  $A_l$  can be calculated as [53]

$$A_{l} = \frac{1}{2\pi} \int_{0}^{2\pi} \psi(\varphi) e^{-jl\varphi} d\varphi, \tag{7}$$



**Figure 7.** (a) The photograph of the fabricated ultra-broadband metasurface  $(21 \times 21)$  with l = 1 and (b) the experimental setup.

where  $\varphi$  represents the azimuth angle and  $\psi$  is the value of the sampling phase. The calculated OAM purities from figure 5(b) depicted in figure 5(d) are higher than 0.75, which shows that the designed OAM mode l=+1 is the dominant part in the RHCP component of the reflected field at each frequency.

To further investigate the performance of the proposed method, two ultra-broadband OAM generators with different OAM mode numbers (l=-1 and +3) are also designed and simulated. The simulated intensity distributions, phase distributions and the calculated OAM purities are illustrated in figure 6. Amplitude nulls caused by the phase singularity can be clearly observed in figures 6(a) and (d) for the OAM generators. The rotation direction and spiral phase changes are determined by the topological charge, as shown in figures 6(b) and (e), respectively. For the spectral analysis of the generated vortex beam shown in figure 6(b) and (e), a high OAM mode purity of the dominant mode l=-1 (l=3) shown in figure 6(c) and (f) can be obtained.

### 4. Experiments

For experimental verification, the metasurface-based vortex beam generator with l=+1 is fabricated and measured. The front view of the fabricated metasurface and the setup of experimental system are shown in figures 7(a) and (b), respectively. The transmitting antenna is a horn antenna (A-info LB-SJ-60180) operating from 6 to 18 GHz, which is connected to Keysight PNA Microwave Network Analyzer (N5227A) along with the receiving antenna. The distance between the transmitting antenna and the metasurface is 700 mm, and the receiving antenna could scan along x- and y-axes with a distance of 350 mm away from the metasurface.

The near-field experimental results at frequencies from 6 to 18 GHz with a step of 2 GHz are illustrated in figure 8, which can be compared with the numerical results in figure 5. Due to the limited working frequency bandwidth of the transmitting horn, the experimental results exclude results at 20 GHz. It can be seen from figures 5(a), (b) and 8(a), (b) that the numerically simulated results and experimental ones are in good

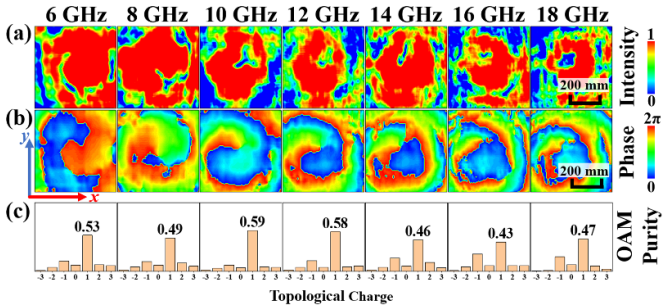


**Figure 8.** The experimental results of the fabricated metasurface with l=+1 from 6 to 18 GHz with a step of 2 GHz. (a) Experimental intensity, (b) phase distributions, and (c) OAM purities in the *xoy* plane.

agreement with each other. The donuts-like intensity profile and the spiral phase distribution can be observed in figures 8(a) and (b), respectively, validating the OAM performance of the fabricated metasurface. Moreover, the calculated OAM purities for l=+1 are around 0.5 for all the observation frequencies. Although the OAM purities are a little less than that in the simulations, the designed OAM mode still occupies the dominant part of the vortex beams as seen in figure 8(c). The discrepancy between the experiments and simulations could be caused by the fabrication tolerance and measurement precision.

### 5. Comparison with other works

To show advantages of the proposed arrow-based fractal metasurface, the comparison with other reported broadband metasurfaces is presented in table 1. Two reported representative works to design multilayer broadband OAM metasurfaces are numbered as [40, 41] for comparisons. As seen, the OAM metasurface in [40] is well optimized to feature a fractional bandwidth of 66.7%, but still with three layers and a large profile. The bilayer metasurface in [41] is designed with the dispersion engineering method for broadband operation with a fractional bandwidth of 86%. Owing to the fact that multilayer broadband OAM metasurfaces are bulky and require complex fabrication processes, several single-layer designs are also proposed. The fractional bandwidths of the rectangular-hole metasurfaces in [42] and the brick-shaped design in [43] are lower than 50%. The ultra-thin single layer metasurface reported in [44] could operate at both transmission and reflection modes simultaneously in a broad fractional band of 112% with a transmission/reflection efficiency of around 0.45. As for the square loop metasurface in [46], the achieved fractional bandwidth is 105% and the efficiency of the meta-atoms is higher than 0.8. In comparison, most of the reported designs are limited either by the bandwidth or the efficiency, and the proposed reflection-type meta-atom in this work features an improved performance with higher efficiency and broader bandwidth, as well as the easy implementation of the single-layer structure.

Mode of Operating Meta-atom Fractional frequency range bandwidth operation Design Layers efficiency 3 66.7% [40] 40-80 GHz >90% Transmission 2 6.95-17.6 GHz >89% 86% Reflection [41] 1 [42] 300-500 THz >50% 50% Transmission [43] 1 18-28 GHz >90% 43.5% Reflection Transmission/Reflection [44] 1 9.3-32.5 GHz  $\sim 45\%$ 112% [45] 1 7.3-21 GHz >92% 96.8% Reflection 6.75-21.85 GHz 105% Reflection [46] 1 >80% Reflection This work 6-19.7 GHz >90% 107% 1

**Table 1.** Comparison for wideband efficient metasurfaces proposed recently.

### 6. Conclusion

In summary, an arrow-based fractal metasurface has been proposed to realize high-efficiency ultra-broadband OAM generators. The proposed reflection-type meta-atom could achieve the co-polarization reflection amplitudes higher than 0.9 under the CP illumination with a fractional bandwidth of 107.2% from 6 to 19.7 GHz. Based on the proposed meta-atom, highperformance OAM generating metasurface arrays with different topological charges are designed and numerically studied. Moreover, to verify the proposed arrow-based fractal meta-atom, the OAM metasurface with l = +1 is fabricated and measured. The experimental results agree well with the simulated results. The proposed method features low cost, easy integration to optical or wireless communication systems, and flexible extension to other frequency regimes. However, due to the fabrication tolerance, the evolving process could be limited to the first several stages. In addition, as other passive devices, the functionality of the metasurface could not be altered after design and fabrication. Nevertheless, the proposed method can be a promising candidate for high capacity data rate communication systems and other fields.

### Data availability statement

The data that support the findings of this study are available upon reasonable request from the authors.

### **Acknowledgments**

This work was supported by the National Natural Science Foundation of China under Grant 62171186, Shanghai Pujiang Program (Grant 18PJ1403200), Fundamental Research Funds for Central Universities, and a research grant from the U S National Science Foundation (1661749).

### **ORCID iD**

Yiting Liu https://orcid.org/0000-0003-1046-6763

### References

- [1] Gibson G, Courtial J, Padgett M J, Vasnetsov M, Pas'ko V, Barnett S M and Franke-Arnold S 2004 Free-space information transfer using light beams carrying orbital angular momentum *Opt. Express* 12 5448
- [2] Winters J 1987 On the capacity of radio communication systems with diversity in a rayleigh fading environment *IEEE J. Sel. Areas Commun.* 5 871
- [3] Zhang Z, Zheng S, Chen Y, Jin X, Chi H and Zhang X 2016 The capacity gain of orbital angular momentum based multiple-input-multiple-output system *Sci. Rep.* 6 25418
- [4] Wang J et al 2012 Terabit free-space data transmission employing orbital angular momentum multiplexing Nat. Photon. 6 488–96
- [5] Zhang K, Wang Y, Yuan Y and Burokur S N 2020 A review of orbital angular momentum vortex beams generation: from traditional methods to metasurfaces Appl. Sci. 10 1015
- [6] Zhang Q, Wang H, Liu L and Teng S 2018 Generation of vector beams using spatial variation nanoslits with linearly polarized light illumination Opt. Express 26 24145
- [7] Mahmouli F E and Walker S D 2013 4-Gbps uncompressed video transmission over a 60-GHz orbital angular momentum wireless channel *IEEE Wirel. Commun. Lett.* 2 223-6
- [8] Yan Y et al 2014 High-capacity millimetre-wave communications with orbital angular momentum multiplexing Nat. Commun. 5 4876
- [9] Yao A M and Padgett M J 2011 Orbital angular momentum: origins, behavior and applications Adv. Opt. Photon. 3 161
- [10] Willner A E *et al* 2015 Optical communications using orbital angular momentum beams *Adv. Opt. Photon.* **7** 66
- [11] Bozinovic N, Yue Y, Ren Y, Tur M, Kristensen P, Huang H, Willner A E and Ramachandran S 2013 Terabit-scale orbital angular momentum mode division multiplexing in fibers Science 340 1545
- [12] Beijersbergen M W, Allen L, Van Der Veen H E L O and Woerdman J P 1993 Astigmatic laser mode converters and transfer of orbital angular momentum *Opt. Commun.* 96 123–32
- [13] Beijersbergen M W, Coerwinkel R P C, Kristensen M and Woerdman J P 1994 Helical-wavefront laser beams produced with a spiral phaseplate Opt. Commun. 112 321–7
- [14] Uchida M and Tonomura A 2010 Generation of electron beams carrying orbital angular momentum *Nature* 464 737–9
- [15] Hui X, Zheng S, Hu Y, Xu C, Jin X, Chi H and Zhang X 2015 Ultralow reflectivity spiral phase plate for generation of millimeter-wave OAM beam *Antennas Wirel. Propag. Lett.* 14 966–9
- [16] Schemmel P, Pisano G and Maffei B 2014 A modular spiral phase plate design for orbital angular momentum generation at millimetre wavelengths *Opt. Express* 22 14712

- [17] Brasselet E, Malinauskas M, Žukauskas A and Juodkazis S 2010 Photopolymerized microscopic vortex beam generators: precise delivery of optical orbital angular momentum Appl. Phys. Lett. 97 211108
- [18] Zhu L and Wang J 2015 Arbitrary manipulation of spatial amplitude and phase using phase-only spatial light modulators Sci. Rep. 4 7441
- [19] Bagnoud V and Zuegel J D 2004 Independent phase and amplitude control of a laser beam by use of a single-phase-only spatial light modulator *Opt. Lett.* 29 295
- [20] Zhou J, Liu Y, Ke Y, Luo H and Wen S 2015 Generation of Airy vortex and Airy vector beams based on the modulation of dynamic and geometric phases Opt. Lett. 40 3193
- [21] Ngcobo S, Litvin I, Burger L and Forbes A 2013 A digital laser for on-demand laser modes *Nat. Commun.* **4** 2289
- [22] Lin D, Daniel J M O and Clarkson W A 2014 Controlling the handedness of directly excited Laguerre–Gaussian modes in a solid-state laser Opt. Lett. 39 3903
- [23] Kim D J and Kim J W 2015 Direct generation of an optical vortex beam in a single-frequency Nd: YVO\_4laser Opt. Lett. 40 399
- [24] Bai Q, Tennant A and Allen B 2014 Experimental circular phased array for generating OAM radio beams *Electron*. Lett. 50 1414–5
- [25] Lei X Y and Cheng Y J 2017 High-efficiency and high-polarization separation reflectarray element for OAM-folded antenna application *Antennas Wirel. Propag. Lett.* 16 1357–60
- [26] Karimi E, Schulz S A, De Leon I, Qassim H, Upham J and Boyd R W 2014 Generating optical orbital angular momentum at visible wavelengths using a plasmonic metasurface *Light: Sci. Appl.* 3 e167
- [27] Mehmood M Q et al 2016 Visible-frequency metasurface for structuring and spatially multiplexing optical vortices Adv. Mater. 28 2533–9
- [28] Jin J, Luo J, Zhang X, Gao H, Li X, Pu M, Gao P, Zhao Z and Luo X 2016 Generation and detection of orbital angular momentum via metasurface Sci. Rep. 6 24286
- [29] Guo Y, Yan L, Pan W and Luo B 2016 Generation and manipulation of orbital angular momentum by all-dielectric metasurfaces *Plasmonics* 11 337–44
- [30] Genevet P, Yu N, Aieta F, Lin J, Kats M A, Blanchard R, Scully M O, Gaburro Z and Capasso F 2012 Ultra-thin plasmonic optical vortex plate based on phase discontinuities Appl. Phys. Lett. 100 013101
- [31] Kang M, Feng T, Wang H T and Li J 2012 Wave front engineering from an array of thin aperture antennas Opt. Express 20 15882
- [32] Patel S K, Charola S, Jadeja R, Nguyen T K and Dhasarathan V 2021 Wideband graphene-based near-infrared solar absorber using C-shaped rectangular sawtooth metasurface *Physica* E **126** 114493
- [33] Charola S, Patel S K, Dalsaniya K, Jadeja R, Nguyen T K and Dhasarathan V 2021 Numerical investigation of wideband L-shaped metasurface based solar absorber for visible and ultraviolet region *Physica* B 601 412503
- [34] Patel S K, Charola S, Parmar J, Ladumor M, Ngo Q M and Dhasarathan V 2020 Broadband and efficient graphene solar absorber using periodical array of C-shaped metasurface Opt. Quantum Electron. 52 250
- [35] Jadeja R, Charola S, Patel S K, Parmar J, Ladumor M, Nguyen T K and Dhasarathan V 2020 Numerical investigation of graphene-based efficient and broadband

- metasurface for terahertz solar absorber *J. Mater. Sci.* **55** 3462–9
- [36] Huang L, Chen X, Mühlenbernd H, Li G, Bai B, Tan Q, Jin G, Zentgraf T and Zhang S 2012 Dispersionless phase discontinuities for controlling light propagation *Nano Lett.* 12 5750–5
- [37] Li J, Chen S, Yang H, Li J, Yu P, Cheng H, Gu C, Chen H T and Tian J 2015 Simultaneous control of light polarization and phase distributions using plasmonic metasurfaces *Adv. Funct. Mater.* **25** 704–10
- [38] Grady N K, Heyes J E, Chowdhury D R, Zeng Y, Reiten M T, Azad A K, Taylor A J, Dalvit D A R and Chen H-T 2013 Terahertz metamaterials for linear polarization conversion and anomalous refraction *Science* 340 1304–7
- [39] Li X, Xiao S, Cai B, He Q, Cui T J and Zhou L 2012 Flat metasurfaces to focus electromagnetic waves in reflection geometry Opt. Lett. 37 4940
- [40] Zhang D, Lin Z, Liu J, Zhang J, Zhang Z, Hao Z C and Wang X 2020 Broadband high-efficiency multiple vortex beams generated by an interleaved geometric-phase multifunctional metasurface Opt. Mater. Express 10 1532
- [41] Xu H X, Liu H, Ling X, Sun Y and Yuan F 2017 Broadband vortex beam generation using multimode Pancharatnam–Berry metasurface *IEEE Trans. Antennas Propag.* 65 7378–82
- [42] Zhang Y, Liu W, Gao J and Yang X 2018 Generating focused 3D perfect vortex beams by plasmonic metasurfaces Adv. Opt. Mater. 6 1701228
- [43] Lin Z, Ba Z and Wang X 2020 Broadband high-efficiency electromagnetic orbital angular momentum beam generation based on a dielectric metasurface *IEEE Photonics J.* 12 4600611
- [44] Akram M R, Ding G, Chen K, Feng Y and Zhu W 2020 Ultrathin single layer metasurfaces with ultra-wideband operation for both transmission and reflection Adv. Mater. 32, 1907308
- [45] Chen W, Gou Y, Ma H, Niu T and Mei Z 2021 High-performance and ultra-broadband vortex beam generation using a Pancharatnam–Berry metasurface with an H-shaped resonator J. Appl. Phys. 54 255101
- [46] Yang L J, Sun S and Sha W E I 2020 Ultrawideband reflection-type metasurface for generating integer and fractional orbital angular momentum *IEEE Trans. Antennas Propag.* 68 2166–75
- [47] Gao L H et al 2015 Broadband diffusion of terahertz waves by multi-bit coding metasurfaces Light: Sci. Appl. 4 e324
- [48] Dhar S, Ghatak R, Gupta B and Poddar D R 2013 A wideband minkowski fractal dielectric resonator antenna *IEEE Trans*. *Antennas Propag.* 61 2895–903
- [49] Zheng Q, Guo C, Vandenbosch G A E, Yuan P and Ding J 2019 Ultra-broadband and high-efficiency reflective polarization rotator based on fractal metasurface with multiple plasmon resonances Opt. Commun. 449 73–78
- [50] Pancharatnam S 1956 Generalized theory of interference, and its applications *Proc. Indian Acad. Sci.* A 44 247–62
- [51] Berry M V 1984 Quantal phase factors accompanying adiabatic changes Proc. R. Soc. A 392 45–57
- [52] Ji C, Song J, Huang C, Wu X and Luo X 2019 Dual-band vortex beam generation with different OAM modes using single-layer metasurface Opt. Express 27 34
- [53] Huang Y, Li X, Li Q, Qi Z, Zhu H, Akram Z and Jiang X 2019 Generation of broadband high-purity dual-mode OAM beams using a four-feed patch antenna: theory and implementation Sci. Rep. 9 12977